

Detailed Single-Molecule Spectroelectrochemical Studies of the Oxidation of Conjugated Polymers

Rodrigo E. Palacios,[†] Wei-Shun Chang,[†] John K. Grey,[†] Ya-Lan Chang,[†] William L. Miller,[†] Chun-Yaung Lu,[†] Graeme Henkelman,[†] Danny Zepeda,[‡] John Ferraris,[‡] and Paul F. Barbara^{*,†}

Department of Chemistry and Biochemistry and the Center for Nano- and Molecular Science and Technology, University of Texas at Austin, Austin, Texas 78712, and Department of Chemistry and the Alan G. McDiarmid NanoTech Institute, University of Texas at Dallas, Richardson, Texas 75083-0688

Received: July 16, 2009; Revised Manuscript Received: September 3, 2009

Single-particle fluorescence spectroelectrochemistry was used to investigate the electrochemical oxidation of isolated, immobilized particles of the conjugated polymers BEH-PPV and MEH-PPV at an indium tin oxide (ITO) electrode immersed in an electrolyte solution. Two types of particles were investigated: (i) polymer single molecules (SM) and (ii) nanoparticle (NP) aggregates of multiple polymer single molecules. For the BEH-PPV polymer, the observation of nearly identical lowest oxidation potentials for different SM in the ensemble is evidence for effective electrostatic screening by the surrounding electrolyte solution. A combination of Monte Carlo simulations and application of Poisson–Boltzmann solvers were used to model the charging of polymer single molecules and nanoparticles in the electrochemical environment. The results indicate that the penetration of electrolyte anions into the polymer nanoparticles is necessary to produce the observed narrow fluorescence quenching vs oxidation potential curves. Finally, fluorescence-lifetime single-molecule spectroelectrochemical (SMS-EC) data revealed that at low potential an excited state *reduction* process (i.e., electron transfer from ITO to the polymer) is probably the dominant fluorescence quenching process.

1. Introduction

Electrochemical (EC) characterization of conjugated polymer thin-film coated electrodes offers unique molecular level information on a number of processes and properties that underlie the function of these materials in electronic devices,^{1–5} such as light emitting diodes (OLEDs),^{6–8} solar cells,^{9,10} field effect transistors (OFETs),^{11–13} bioelectronics sensors,¹⁴ and electrochemical energy storage devices.¹⁵ In an electrochemical cell, the potential difference (E) between the working electrode and a reference electrode in the electrolyte solution is controlled by employing a counter electrode and a potentiostat.¹⁶ At the working electrode, an electrochemical double layer is formed in which the excess charge on the electrode surface is compensated by an accumulation of electrolyte ions of the opposite charge. This charging of the double layer produces a large change in the electrical potential on the angstrom scale, which in turn makes redox processes at the electrode thermodynamically favorable and kinetically accessible, at the appropriate E . In an electrochemical experiment, the instantaneous current flowing at the working electrode—due to the reduction—oxidation (redox) processes and double layer capacitive charging—is recorded as a function of time, while a time-dependent electrode potential difference, E , is applied across the double layer.

We are especially concerned in this paper with electrochemical oxidation of conjugated polymers, i.e., the removal of an electron from a neutral conjugated polymer by the working electrode to produce a positive carrier (or hole polaron) in the polymer film. Electrochemical measurements of oxidation processes at working electrodes that are continuously coated

with semiconducting conjugated polymer are complicated by the disruption of the electrochemical double layer by the polymer at the working electrode, resulting from poor mobility of electrolyte ions in the conjugated polymer film. For typical nonpolar conjugated polymers, the neutral state of the film is both solvent and ion free. This ionic insulating effect can be minimized by the so-called “break-in” phenomenon. Break-in occurs after cycling the potential for multiple cycles, which induces electroporation of the film allowing the penetration of electrolyte ions and solvent molecules into the film and formation of the double layer at the electrode surface. Furthermore, to complete the redox process of the interior of the conjugated polymer film, electrolyte ions must enter the polymer film to compensate the charge of the carriers produced by the oxidation.^{16,17} The latter process can be viewed as a type of ion-gated electron transfer.^{18–22}

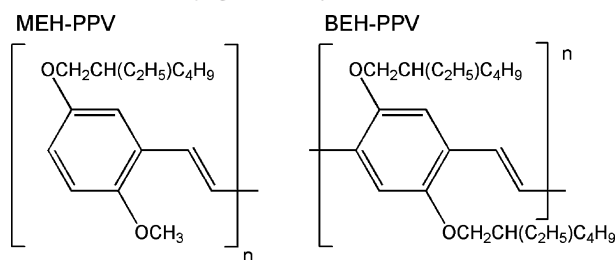
We have recently shown that working electrodes coated with isolated conjugated polymer particles (either single conjugated polymer molecules or nanoparticle aggregates of multiple polymer chains) offer a powerful geometry to investigate the fast kinetics of conjugated polymer oxidation without dynamical distortions due to break-in since each particle in this geometry is in contact with an undisrupted double layer. In this paper, we use SMS-EC on the conjugated polymers poly[2,5-(2'-ethylhexyloxy)]-1,4-phenylenevinylene, BEH-PPV, and poly[2-methoxy-5-(2'-ethylhexyloxy)]-1,4-phenylenevinylene, MEH-PPV (see Scheme 1).^{23–26} The ultrasensitive, indirect electrochemical technique, single-molecule spectroelectrochemistry (SMS-EC),^{27–29} is used to indirectly investigate the electrical oxidation of isolated single polymer molecules (SM) of 1500–4000 repeat units and nanoparticle (NP) aggregates of 10–250 polymer chains at the interface of the widely used electrode material, indium tin oxide (ITO) in an electrochemical cell (see Figure 1). In SMS-EC, charge injection is indirectly measured from charge-induced

* Corresponding author. E-mail: p.barbara@mail.utexas.edu.

[†] University of Texas at Austin.

[‡] University of Texas at Dallas.

SCHEME 1: Conjugated Polymers Chemical Structure



fluorescence quenching of emitting particles immobilized on an electrode surface. The advantage of SMS-EC is that its ultrahigh sensitivity allows for *the monitoring of the injection of the first few (or even single) positive charges* into the ground electronic states of single conjugated polymer molecules one molecule at a time during reversible oxidation at a working electrode. This technique has allowed us to record the distribution of the potentials required to inject one charge for each single molecule for a large ensemble of molecules, offering new information on the heterogeneity of the oxidation process of conjugated polymers at the molecular level.

SMS-EC is also used in this work to investigate the ground-state oxidation of nanoparticles (NPs, radii = 15–40 nm) of BEH-PPV in contact with ITO offering information on charge trapping. The SMS-EC NP data, when analyzed in combination with theoretical modeling, demonstrated that solvent and electrolyte ions rapidly penetrate into the NP during oxidation. We also use SMS-EC on NP to investigate deeply trapped holes (DTH) in conjugated polymers. DTH can significantly affect

the charge injection and transport properties (e.g., hole mobilities) of the materials and interfaces and thus influence device performance.^{7,30–40} In particular, we investigate the mechanism for the formation and removal of DTH, the effect of optical excitation on DTH removal dynamics, and whether DTH are present at equilibrium in “pristine” NP materials.

Finally, SMS-EC in combination with picosecond time-resolved fluorescence detection was employed in this paper to study the redox reactions of MEH-PPV conjugated polymer SM in their excited states at electrodes.

2. Experimental Section

Materials. Poly[(2-methoxy-5-(2'-ethylhexyloxy))-1,4-phenylenevinylene (MEH-PPV, MW = 1000 kg/mol, PDI = 4) was purchased from American Dye Source Inc. All solvents used were HPLC grade or better and were used without further purification. Polystyrene (PS, MW = 240 kg/mol), acetonitrile (MeCN), toluene, tetrahydrofuran (THF), and lithium perchlorate (LiClO₄) were purchased from Sigma-Aldrich. Nafion (perfluorosulfonic acid-PTFE copolymer, with Li⁺ counterions) was purchased from Alfa Aesar. ITO coated coverslips were purchased from Metavac and cleaned by sonication for 15 min in trichloroethylene, acetone, and finally methanol. The cleaned ITO substrates were stored in methanol and dried in a nitrogen stream immediately before spin-coating.

Silver wire (25 μm diameter) was purchased from Alfa Products. Poly[(2,5-bis(2'-ethylhexyloxy))-1,4-phenylenevinylene (BEH-PPV, MW = 544 kg/mol, PDI = 1.8) was synthesized as described below, and the monomer of BEH-PPV was synthesized according to the literature with slight modifications.^{41,42}

1,4-Bis(2'-ethylhexyloxy)benzene. Potassium hydroxide (509 mmol) was dissolved in DMSO (150 mL) in a 250 mL 3-neck round-bottom flask under a blanket of nitrogen. Hydroquinone (182 mmol) was then added, and the mixture was stirred for a half hour at room temperature, followed by addition of 2-ethylhexylbromide (478 mmol). The reaction was stirred under nitrogen at room temperature overnight. The next day the organic layer was separated and washed three times with 100 mL of DI water. The organic layer was dried over magnesium sulfate. The solvent was removed under reduced pressure, and the residue was purified by column chromatography (basic alumina, hexanes) to afford 47 g (78% yield) of yellow oil. ¹H NMR (CDCl₃, 270 MHz): δ 6.86 (s, 4H, C^{ar}-H), 3.84–3.81 (d, 4H, O-CH₂), 1.8–1.65 (m, 2H, O-CH₂-CH-), 1.6–1.2 (m, 18H, other CH₂), 0.97–0.95 (t, 12H, CH₃). ¹³C NMR (CDCl₃, 270 MHz): δ 153.5 (s, C^{ar}-O), 115.4 (s, C^{ar}-H), 71.2 (s, O-CH₂), 39.6 (s, O-CH₂-CH-), 30.6 (s, CH₂), 28.9, 23.9, 23.2 (s, CH₂), 14.2 (s, CH₃), 11.2 (s, other CH₃).

Synthesis of α,α'-Dibromo-2,5-bis(2'-ethylhexyloxy)xylene. 1,4-Bis(2'-ethylhexyloxy)benzene (45 g, 135 mmol) was added to a suspension of paraformaldehyde (19.4 g, 647 mmol) and glacial acetic acid (25 mL) in a 250 mL round-bottom flask. The suspension was stirred for 15 min at room temperature, and then 117 mL of 33% HBr in acetic acid (646 mmol) was added at once. The reaction was then heated to 80 °C for 5 h. The reaction mixture was cooled to room temperature, and crude was partitioned between water and chloroform. The aqueous layer was back-extracted with chloroform, and the organic phase washed with 7% sodium carbonate three times. The organic phase was dried over magnesium sulfate, followed by the removal of the solvent under reduced pressure. Crystallization from isopropyl alcohol afforded 23 g (42% yield) of white solid; mp = 63.5–65 °C. ¹H NMR (CDCl₃, 270 MHz): δ 6.84 (s, 2H, C^{ar}-H), 4.51 (s, 4H, CH₂-Br), 3.91–3.82 (d, 4H, O-CH₂),

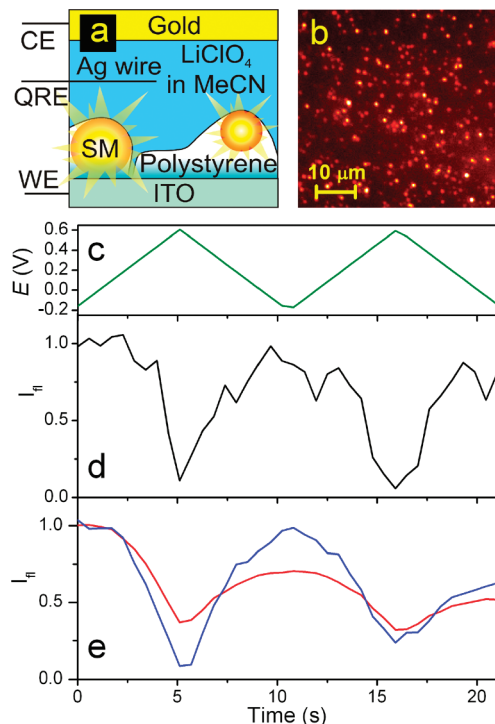


Figure 1. (a) SMS-EC cell diagram. (b) Wide-field fluorescence image of an SMS-EC cell. (c) Applied electrochemical potential. (d) Normalized BEH-PPV single-molecule fluorescence intensity trajectory obtained in an SMS-EC cell while applying the potential shown in (c). (e) Ensemble average of normalized BEH-PPV single-molecule fluorescence-intensity trajectories (red, 810 trajectories) and subensemble (blue) constructed by sorting trajectories with normalized intensities lower than 0.2 in the 5–6 s time range and higher than 0.8 in the 10–11 s time range (75 trajectories).

1.8–1.65 (m, 2H, O–CH₂–CH–), 1.6–1.20 (m, 18H, CH₂), 0.97–0.94 (t, 12H, CH₃). ¹³C NMR (CDCl₃, 270 MHz): δ 138.3 (s, C^{ar}–C), 150.7 (s, C^{ar}–O), 127.4 (s, C^{ar}–H), 115 (s, C^{ar}–C), 71.2 (s, O–CH₂), 39.6 (s, O–CH₂–CH–), 30.7 (s, CH₂), 29.2, 24.1, 23.1 (s, CH₂), 14.2 (s, CH₃), 11.1 (s, other CH₃).

Polymerization Procedure. BEH-PPV was synthesized through the “reversed” Gilch polymerization route (addition of the monomer solution to a potassium *tert*-butoxide/initiator solution).^{41,43}

Weighing and transfer of the reagents were performed inside a nitrogen-filled glovebox. Potassium *tert*-butoxide (1.47 g, 13 mmol) and *p*-methoxyphenol (8.6 mg, 2.4 mol %) were dissolved in anhydrous THF (120 mL) in a 250 mL round-bottom flask, and it was then removed from the glovebox. An IKA Euro-star mechanical stirrer was attached keeping the flask flushed with nitrogen. The mixture was stirred at 300 rpm while keeping the flask inside an isopropanol/liquid nitrogen bath (–35 °C). BEH-PPV monomer (1.5 g, 2.9 mmol) was dissolved in anhydrous THF (10 mL) and was injected at a rate of 20 mL/h using a KDS (series 200) syringe pump. Stirring and cooling was continued one hour after monomer addition was complete. The red polymer was collected on a Millipore Durapore 0.45 μm membrane filter after precipitation from methanol and dried under vacuum overnight at 50 °C. The polymer was then dissolved in THF and precipitated again in methanol and subjected to a hexane Soxhlet extraction. The red polymer strands were collected and dried under vacuum to give 0.83 g (80% yield) of BEH-PPV. ¹H NMR (270 MHz, CDCl₃): δ 7.75–7.41 (d, 1.2H), 4.27–3.75 (t, 4H), 1.93–1.73 (t, 2H), 1.70–0.45 (m, 28H). UV–visible absorption (CHCl₃) λ_{max}: 505 nm. Emission (CHCl₃) λ_{max}: 557 nm. GPC (THF) M_w = 544 kDa; PDI = 1.8. FT-IR (polymer film) (cm^{–1}): 472, 723, 772, 1586, 1692, 1804, 1830, 2031, 2221, 2316, 2601, 2668, 2731, 2974.

SMS-EC Setup. The EC cells used in these experiments were constructed from a planar transparent ITO working electrode, a planar gold counter electrode, and a silver wire quasi-reference electrode (AgQRE), which was inserted in the gap between the two planar electrodes (see Figure 1a, for details on the cell assembly and configuration).^{27–29} For single-molecule samples, the transparent ITO electrode was spin-coated with a thin discontinuous PS layer interspersed with single conjugated-polymer (CP) chains that were spatially well resolved. For nanoparticle samples, two approaches were used to distribute the CP NPs onto the ITO electrode. The first approach used a 20–80 nm film of Nafion as the supporting host polymer. In the second approach, the NPs were directly cast on the ITO electrode without the supporting host polymer. Nanoparticles were prepared by a reprecipitation technique as described elsewhere.^{28,29,44–46} Water^{28,44} and dry cyclohexane²⁹ were used as the nonsolvents for particle formation. Single molecules and particles were present in their corresponding layers in a spatial distribution ranging from 0.1 to 1 particles/μm² depending on sample preparation conditions. The gap between the planar electrodes was filled with a MeCN solution containing 0.1 M supporting electrolyte, LiClO₄. The time dependence of hundreds of individual fluorescent “spots”, *I*_{fl}(*t*), each due to a SM or NP, was determined from images that were recorded at fixed time intervals by a wide field microscope (NIKON-Eclipse TE2000; equipped with a ROPER SCIENTIFIC-Cascade 512B, CCD camera) using 488 nm excitation (see Figure 1b). Images were acquired using the commercially available program Metamorph (Molecular Devices, 1994, Version 6.2r6). A home-written Matlab routine was used to find the individual bright

spots (due to SM or NP) in the CCD images and to calculate the integrated fluorescence intensities of the spots.

For both the linearly scanned and pulsed SMS-EC experiments, the timing of the collection of the fluorescence images was synchronized with the time-varying electrochemical potential, *E*(*t*), of the working electrode (see Figure 1c). *E*(*t*) was maintained at the required potential relative to the reference electrode (AgQRE) by a potentiostat (Autolab, PGSTAT 100) and is reported herein relative to the ferrocene/ferrocenium (Fc/Fc⁺) couple (introduced into the cell after the SMS-EC data were acquired) unless otherwise noted. Potentials relative to Fc/Fc⁺ are about 0.20 ± 0.04 V more negative than to AgQRE.

Conventional Electrochemistry. Cyclic voltammetry (CV) experiments on BEH-PPV thin films (~15–25 nm) were carried out in SMS-EC cells constructed as described above except that the films were spun cast over ITO substrates from toluene solutions of the polymers (~1.7 mg/mL). Potential scan rates were as indicated in the figure captions.

Time-Resolved Spectroelectrochemistry. Potential-dependent, time-resolved fluorescence emission intensities of PPV derivatives were measured on a confocal scanning microscope that has been described elsewhere.⁴⁷ Single photon counting detection was performed with a fast response avalanche photodiode (id Quantique, id100–50), and excitation of single molecules in the EC device was achieved by using the frequency doubled output of a Ti:sapphire laser (Coherent, Mira 900, 488 nm, 76 MHz, ~200 fs). Decay curves were constructed using a time-correlated single-photon counting board (Becker&Hickl, SPC 630), and photons were routed into separate channels depending on the sign of the applied square wave potential to generate potential-dependent decay curves. Typical sweep ranges and rates were –0.4–0.4 V and 1 V/s, respectively.

3. Results and Discussion

3.1. Basic SMS-EC Experiment. Figure 1d shows a typical BEH-PPV single-molecule fluorescence-intensity trajectory acquired in an SMS-EC cell while applying an electrochemical potential (*E*, green curve on panel c) to the ITO working electrode. The figure shows that when *E* reaches ~0.5 V the fluorescence intensity of a single BEH-PPV chain, i.e., SM, decreases rapidly until it is almost fully quenched, and when *E* is scanned back to 0 V, the chain recovers its initial emission intensity. The decrease of fluorescence intensity at *E* > 0.5 V is assigned to exciton quenching induced by holes (radical cations) formed by electrochemical oxidation of redox units in the polymer chain.^{27,48,49} When *E* is scanned back to 0 V, the recovery of the initial fluorescence intensity is associated with the electrochemical reduction (neutralization) of holes to yield the original uncharged redox units. Previous studies from our laboratory indicate that one hole (i.e., oxidized unit) quenches approximately 40–60% of the fluorescence intensity of an individual polymer chain.^{48–51} This highly efficient quenching relationship makes SMS-EC an ultrasensitive technique for detecting EC oxidation events, allowing for the measurement of the injection of one or a few elementary charges at a time into a single polymer chain. Figure 1e shows the total ensemble (red curve) and a subensemble (blue curve) of single-molecule fluorescence-intensity transients. The ensemble data indicate that some molecules do not show complete fluorescence quenching at the highest applied potential (*E*_{max} = 0.6 V) and/or complete fluorescence recovery after the first potential cycle (*t* ~ 11 s). The lack of full fluorescence quenching in the ensemble data is due to the presence of molecules that are not in good electronic contact with the EC double layer and consequently show poor

EC charging under these conditions. The lack of full fluorescence recovery for some molecules is assigned to a subsequent chemical reaction (e.g., deprotonation or reaction with dioxygen)¹⁶ that occurs after EC oxidation. This subsequent chemical reaction produces an unknown reacted site in the polymer chain that quenches fluorescence. Although this chemical reaction is quite ubiquitous among the studied polymer materials and experimental conditions, we find examples of reversible oxidation in a significant fraction of the studied molecules. The blue subensemble curve shown in Figure 1e was constructed by sorting molecules that show higher than 95% fluorescence quenching and recovery during the first potential cycle. Approximately 10% of the studied molecules show this reversible fluorescence quenching behavior. The fraction of molecules showing reversible oxidation increases with increasing potential scan rate and decreases with increasing E_{\max} consistent with the idea of an irreversible reaction competing with the reduction of the oxidized polymer.

3.2. Redox-Accessible Density of States of Conjugated Polymers. A key concept implied by previous electrochemical studies of conjugated polymers is that the redox processes involve localized redox accessible sites along the polymer backbone that correspond to polymer segments in which conjugation is preserved. In detail, the postbreak-in, “lowest” or “first” electrochemical oxidation wave of bulk conjugated polymer thin films at electrodes has been assigned to the sum of the “lowest” oxidation waves for each of the various redox accessible sites. (This is closely analogous to standard interpretation of the electronic absorption spectra of conjugated polymers which ascribes the spectra to the sum of the lowest-energy absorption bands of different localized chromophores along the polymer backbone.)

Assuming the validity of the localized redox accessible state picture, a particularly important electrochemical property of conjugated polymers is the distribution $p(E_{1/2})$ of the lowest oxidation potentials ($E_{1/2}$) of the various localized redox accessible states of the bulk polymer. Note $E_{1/2}$ refers to an extent of oxidation, i.e., 50%, in analogy to the half-filled level definition of the Fermi level for semiconductors. The $p(E_{1/2})$ distribution closely parallels the localized density of states $p(E_{\text{HOMO}})$ of the highest occupied molecular orbital energies (HOMO) of a “dry” conjugated polymer film. The mean value, width, and functional form of $p(E_{\text{HOMO}})$ are critically important factors in controlling the functional properties of conjugated polymers, e.g., charge mobilities and barrier for charge transfer across polymer/inorganic electrode interfaces. Simply speaking, $p(E_{1/2})$ and $p(E_{\text{HOMO}})$ differ primarily due to the solvation energy of the oxidized localized states in the electrochemical case, electrostatic screening due to the electrolyte, the use of different reference energy, and conformational and packing effects on the local electronic energy of the polymer.

Establishing in detail the energy and shape of the $p(E_{1/2})$ and $p(E_{\text{HOMO}})$ distributions is important for the successful application of conjugated polymers in organic electronic devices and in elucidating various factors that modulate the energetics of polymer oxidation and reduction in different environments. On the basis of the current understanding of the electronic energy levels of conjugated polymers, to a first approximation, $p(E_{1/2})$ and $p(E_{\text{HOMO}})$ should be related to the distribution of conjugation length of such segments (i.e., redox units). A variety of factors (e.g., electron correlation effects, thermal disorder, and packing-induced torsion) limit the maximum effective conjugation length,^{52–55} creating an energy-level accumulation effect in the low-energy edge of the HOMO band. This pile-up effect should

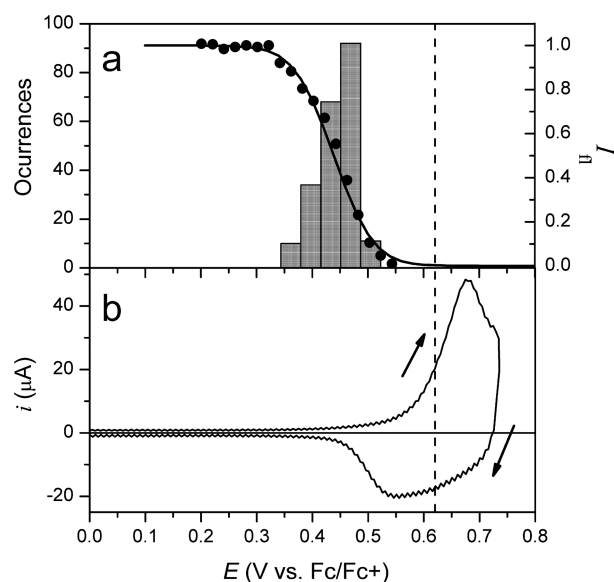


Figure 2. (a) Distribution of potentials at which the fluorescence of individual particles is quenched by half ($E_{1/2,SM,Q}$) for 215 BEH-PPV single molecules (bars, left axis). Ensemble of 215 normalized single-molecule fluorescence-intensity trajectories (data points) and corresponding fit (black curve) (details of the model are in the text). Simulation parameters are shown in Table 1. (b) Cyclic voltammogram of a BEH-PPV film (~ 20 nm) on an ITO electrode. Conditions: 0.5 V/s sweep rate, acetonitrile solution containing 0.1 M LiClO_4 . The dotted vertical line indicates the position of the estimated $E_{1/2}$ from the CV measurement (0.62 V).

lead to a narrow distribution of redox accessible states on the low potential edge of $p(E_{1/2})$ and $p(E_{\text{HOMO}})$.

The SMS-EC SM experiments measure the potential, $E_{1/2,SM,Q,k}$, necessary to quench the fluorescence of the “ k ” individual SM by 50%; $E_{1/2,SM,Q,k}$ is the electrochemical analogue of the “first ionization energy” of the k th SM. Since a typical polymer chain in this study is comprised of ~ 100 repeat units, $E_{1/2,SM,Q,k}$ corresponds on average to about 1/100th of a positive charge per redox accessible state, i.e., not the 50%, that is assumed in the definition of $p(E_{1/2})$. If all of the redox accessible states were of equal energy and noninteracting, the half wave oxidation potential of the “ k ” individual SM ($E_{1/2,SM,k}$) would be larger than $E_{1/2,SM,Q,k}$ by ~ 0.12 V due to a simple statistical factor (see below for further details). While $E_{1/2,SM,Q,k}$ does not directly lead to $E_{1/2,SM,k}$, it does offer unprecedented information regarding the most easily oxidized states of the conjugated polymer molecules.

The narrow $E_{1/2,SM,Q}$ distribution (s.d. < 0.03 V) that is observed herein (see Figure 2a bars) implies that the lowest-energy sites on each chain have nearly identical oxidation potentials and that the low-energy “edge” of $p(E_{1/2})$ itself must be sharp. At first glance, the homogeneity of $E_{1/2,SM,Q,k}$ values and sharp low energy edge of $p(E_{1/2})$ are surprising due to the presumably broad distribution of environments due to the heterogeneity of the ITO electrode and the many different energetically accessible conformations of the polymer chain. Apparently, the electrolyte solution surrounding the single polymer chains effectively screens local inhomogeneities in the electrode charge distribution resulting, for example, from surface charges on the ~ 1 nm scale of single oxidizable sites in the SM. On the basis of spectroscopy data for analogous electrolyte free samples, each SM is expected to have a “collapsed”, roughly cylindrical conformation with a long axis on the 10 nm scale.

TABLE 1: Estimated BEH-PPV Oxidation Potential and $E_{1/2}$ Distribution

sample	method	symbol	$E_{1/2}$ [V] ^a	σ [V] ^a
thin film	conventional CV	$E_{1/2,\text{Film}}$	0.62 (0.04)	---
single molecules	model	$E_{1/2,\text{SM}}$	0.54 (0.02)	0.04 (0.02)
single molecules ^b	SMS-EC $E_{1/2}$	$E_{1/2,\text{SM,Q}}$	0.44 (0.01)	0.03 (0.02)
nanoparticles	SMS-EC $E_{1/2}$	$E_{1/2,\text{NP,Q}}$	0.47 (0.01)	0.02 (0.02)
sample type a				

^a Potential measured versus the ferrocene/ferrocenium couple. Parentheses indicate estimated error bars. ^b Parameters shown correspond to the distribution of potentials at which the fluorescence of a single molecule decreases by half.

Characterizing the Low-Energy Edge of $p(E_{1/2})$. The SMS-EC data were analyzed statistically to obtain quantitative information on the lowest-energy edge of $p(E_{1/2})$ for the ensemble of SM. Here the ensemble ($I_{\text{tot}}(E)$) of normalized single-particle fluorescence-intensity (I_{fl}) vs E trajectories was fit using eq 1^{27,28,48,49}

$$I_{\text{tot}}(E) = \frac{\int p(E_{1/2}) I_{\text{fl}}(E_{1/2}) dE_{1/2}}{\int p(E_{1/2}) dE_{1/2}} \quad (1)$$

where $p(E_{1/2})$ is assumed to take the shape of a Gaussian distribution ($\exp[-(E_{1/2} - E_{1/2,\text{mean}})^2/2\sigma^2]$) and $I_{\text{fl}}(E)$ is the normalized fluorescence intensity for individual molecules as a function of bias (E), which has been shown to reflect the number of oxidized chromophores/redox centers (C_{ox}) per particle.^{28,48} In the assumed fast equilibrium limit, C_{ox} is given by the Nernst relationship, and ($I_{\text{fl}}(E)$) can be written as

$$I_{\text{fl}}(E) = \frac{C_{\text{red}}}{C_{\text{tot}}} \left(1 + \frac{\text{QD}}{1 - \text{QD}} \cdot C_{\text{ox}} \right)^{-1} \quad (2)$$

with $C_{\text{red}} = C_{\text{tot}}/(1 + \exp[(E - E_{1/2})/kT])$ and $C_{\text{ox}} = C_{\text{tot}} - C_{\text{red}}$ where QD is the normalized fluorescence quenching depth per oxidized chromophore/redox center; C_{tot} is the total number chromophores/redox centers per molecule; $kT = (26 \text{ mV})^{-1}$ (at room temperature); and $E_{1/2}$ is the half-wave potential for the oxidation of a single redox center. In the case of single molecules, we assume a 50% quenching per oxidized center, 100 redox centers per molecule, and the same $E_{1/2}$ for all centers within a molecule.

The relative concentrations of reduced and oxidized units are calculated based on the applied electrochemical potential (E) using the Nernst relationship, thus assuming a very fast equilibrium between both redox forms. Under these assumptions, the analysis permits the calculation of the distribution of half-wave oxidation potentials for single molecules ($E_{1/2,\text{SM},k}$) by fitting the experimental data. Figure 2a shows the ensemble of normalized single-molecule fluorescence-intensity trajectories (black circles) and the corresponding fits (black curve). The experimental data used for this analysis were sorted so that only single-molecule fluorescence-transients showing reversible oxidation were considered. This selection was done to diminish the contribution of irreversible photochemical and electrochemical reactions to the measured $E_{1/2,\text{SM,Q}}$ distribution and the calculated $E_{1/2,\text{SM}}$ distribution. For simplicity, only the data corresponding to the forward direction of the potential sweep are shown in Figure 2a (the reverse-direction data closely match the forward one in this case). Note that the measured $E_{1/2,\text{SM,Q},k}$ for each molecule corresponds primarily to the redox sites that

are easier to oxidize within that molecule, thus the obtained distribution of $E_{1/2,\text{SM},k}$ can be used as a measure of the low-energy edge of the $p(E_{1/2})$. In addition to the ensemble experimental data and fits, Figure 2a shows the measured $E_{1/2,\text{SM,Q}}$ histogram. As mentioned before, the values in these histograms are indicative of the first oxidation event in each individual molecule. Figure 2b shows the results of conventional cyclic voltammetry (CV) for a BEH-PPV thin film (~ 20 nm) spun cast on ITO for comparison. The dashed line shows the position of the polymer film oxidation potential ($E_{1/2,\text{film}}$) based on the CV measurement. The results from the data and analysis shown in Figure 2 are summarized in Table 1.

As can be observed in Table 1, the estimated mean $E_{1/2,\text{SM}}$ obtained from the data analysis is slightly more negative than the $E_{1/2,\text{film}}$ value obtained by conventional CV measurements. However, the mean $E_{1/2,\text{SM}}$ estimated in this manner is highly dependent on the quenching-per-charge parameter (QD) used in the models for the fitting procedure (e.g., the mean $E_{1/2,\text{SM}}$ is 0.56 V for QD = 0.5 and 0.60 V for QD = 0.8). The fitting procedure yields a narrow Gaussian spread of $E_{1/2,\text{SM}}$ values, $\sigma = 0.04$ V, which is consistent with the expected pile-up effect at the low-energy edge of $P(E_{1/2})$. Note that the shift between the onset of the ensemble of normalized single-molecule fluorescence-quenching curves (Figure 2a) and the $E_{1/2,\text{film}}$ (Figure 2, vertical dash line) is mainly due to a statistical factor resulting from the high quenching effect of a single oxidized chromophore per polymer molecule ($\sim 50\%$).

3.3. BEH-PPV Nanoparticle Oxidation. To further investigate the hole transfer process at the BEH-PPV/ITO interface, we applied the SMS-EC technique to study nanoparticles of this material under different experimental conditions. In the previous description of EC charging and fluorescence-quenching of single BEH-PPV molecules, the penetration of solvent and ions into the polymer particle core during charging had not been considered. Evidence (vide infra) suggests that in larger BEH-PPV nanoparticles ($r = 25 \pm 15$ nm) ion and solvent penetration occurs rapidly during the EC oxidation. Different types of samples were prepared to investigate the effect of the supporting polymer layer in the charge transfer process. Samples of type A were prepared by spin-casting BEH-PPV NPs made in cyclohexane directly over the ITO substrate in the absence of a host polymer. Samples of type B and C were prepared by imbedding NPs made in water in an ion conducting Nafion host polymer layer with a thickness of ~ 20 and 100 nm, respectively.

Figure 3a shows the ensemble average of normalized single BEH-PPV NP fluorescence-intensity trajectories for the three types of samples. In these experiments, the NPs are exposed to potentials higher than the half-wave oxidation potential of bulk BEH-PPV film ($E_{1/2,\text{film}} = 0.62$, see Table 1) for relatively long periods of time. During these periods, a large fraction of particles are highly oxidized (fully quenched), and irreversible chemical reactions occur (as described above) leading to the irreversible fluorescence quenching of these particles. As shown by the green and red ensemble curves in the figure, more than 99% of NPs in samples of type A and B show full quenching in a narrow potential range. This observation is consistent with a good electronic contact between NPs and the electrochemical double layer in these samples. The situation is clearly different for samples of type C as shown by the blue ensemble average curve. In these types of samples, two general types of fluorescence behaviors are observed within the applied potential range: (I) complete fluorescence quenching and (II) partial to nonquenching. The fraction of molecules showing either behavior varies significantly from sample to sample, but it is usually higher for

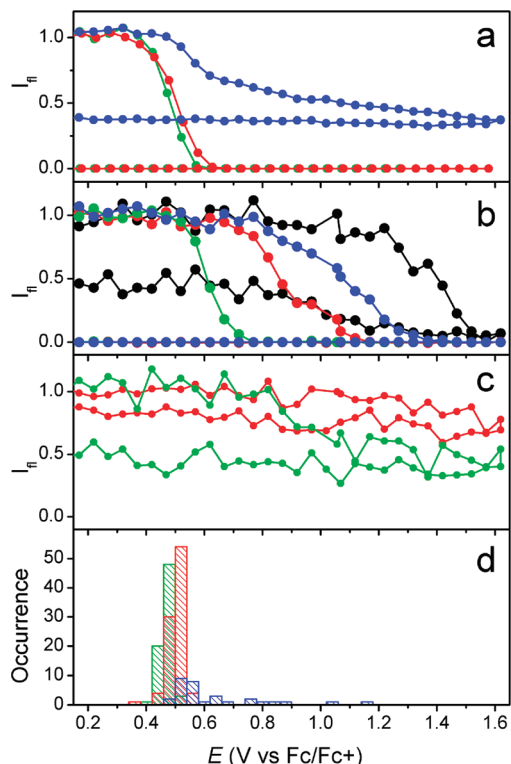


Figure 3. (a) Ensemble of normalized single BEH-PPV NP fluorescence-intensity trajectories (I_{fi}) for samples with different host polymer layers: no-host (72 NPs, green curve), Nafion 25 nm (93 NPs, red curve), Nafion 100 nm (130 NPs, blue curve). (b) Examples of single NP fluorescence transients for the sample with a thick Nafion layer (100 nm) host polymer showing full quenching. (c) Same as (b) for transients that do not show full quenching. (d) SMS-EC $E_{1/2,NP,Q}$ histogram for BEH-PPV NP samples with different host polymer layers: no host (green), Nafion 25 nm (red), Nafion 100 nm (blue). $E_{1/2,NP,Q}$ is defined as the potential at which the fluorescence-intensity of an individual NP drops 50%. Particles that do not show complete quenching within the applied potential range were not considered.

type-II behavior. Figures 3b and 3c show examples of single NP trajectories with type I and II fluorescence behavior, respectively. These data clearly demonstrate the diversity of fluorescence vs potential behaviors observed in type C samples.

Figure 3d shows histograms of the potentials at which the fluorescence intensity of the NP is quenched by half, i.e. $E_{1/2,NP,Q}$, for the three types of samples studied. The data used for the construction of the histograms were sorted to remove particles that do not show full quenching within the applied potential range. For samples of type A and B, the histograms (green and red bars, respectively) show narrow distribution values which fall within ~ 0.2 V from the half wave potential of the bulk polymer film ($E_{1/2,Flm} = 0.62$ V, see Table 1). The observed narrow distribution of $E_{1/2,NP,Q}$ is consistent with good particle/double-layer contact and efficient EC charging for these samples as mentioned before. The fact that the $E_{1/2,NP,Q}$ values for these types of samples are lower than the $E_{1/2}$ of the film indicates that in the NPs, as in the single molecules, the SMS-EC technique gives information about the lower-energy region of the $p(E_{1/2})$. An alternative interpretation for the latter observation is that the effective oxidation potential of the sites in a single NP is lower than that in the films due to the better charge stabilization and smaller electrical resistance to charge in the former. Samples of type C show a $E_{1/2,NP,Q}$ distribution that extends over a large range of potentials (~ 0.5 – 1.2 V) with many values falling above the $E_{1/2}$ of the polymer film (0.62 V) (see Figure 3d, blue bars). This observation is consistent

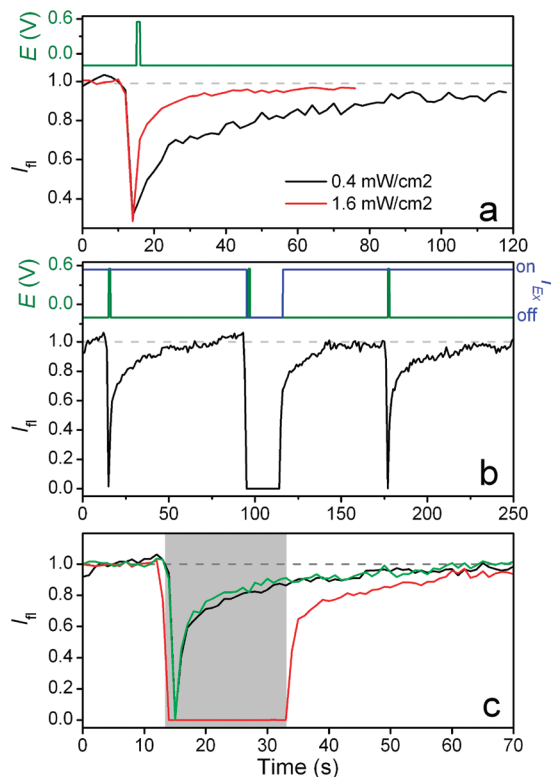


Figure 4. (a) Ensemble average of 33 single BEH-PPV NP normalized fluorescence-intensity trajectories obtained at optical excitation intensities of 0.4 (black) and 1.6 (red) mW/cm^2 while applying the potential function shown by the top black line. (b) Subensemble of single BEH-PPV NP normalized fluorescence-intensity trajectories showing reversible quenching in three consecutive bias pulses. The applied electrochemical potential and optical excitation intensity are shown by the top green and blue curves, respectively. (c) Black, red, and blue traces correspond to the 0–93, 83–176, and 62–260 s periods of the curve shown in (b), respectively. Traces are overlaid on the same time scale so that the relative time for the bias pulse in each of the traces is matched; the gray area shows the light-off time interval corresponding to the red trace.

with a large fraction of the NPs being separated from the EC double-layer by distances large enough so that charging becomes kinetically controlled. Under these conditions, higher EC potentials are needed to achieve charge injection rates fast enough to significantly charge the particles within the time scale of the experiment (<60 s).

Deep Traps in Nanoparticles. The formation and decay of hole traps were studied in BEH-PPV nanoparticles under electrochemical oxidation conditions. The particles were subject to significant oxidation by applying potential pulses (≤ 3 s) with E values close to $E_{1/2,Flm}$ of BEH-PPV. As shown in Figure 4a, ensemble averages of individual particle I_{fi} curves show fast fluorescence quenching during potential-induced oxidative charging. In contrast to this effect, the recovery of the corresponding initial I_{fi} intensity (associated with the rereduction process at -0.15 V) can be very slow (more than 100 s, Figure 4a black curve) and has a wide distribution of recovery times for the individual I_{fi} curves (not shown). The slow fluorescence recovery is associated with the rereduction of hole traps formed during the charging process. The formation of hole traps has been studied previously in F8BT single nanoparticles using a simple model as described elsewhere.²⁸ This model considers the presence of two interconverting redox species/sites, shallow traps (S/S^+), and deep traps (D/D^+) and their corresponding oxidation potentials, $E_{1/2,S}$ and $E_{1/2,D}$. When a particle is held at

$E_{1/2,S}$, the pristine redox centers (shallow sites) are rapidly going between their reduced (S) and oxidized (S^+) states. Deep traps represent some chemical change of S^+ (e.g., deprotonation, dimerization, isomerization, etc.) that leads to the formation of a new oxidized state, D^+ (deep trap), with an oxidation potential ($E_{1/2,D}$) more negative than $E_{1/2,S}$. This new oxidized state reduces back slowly to its neutral form (D) which eventually relaxes to the parent state S.

Another important observation on this type of experiments is that the rate of fluorescence recovery after charge-induced quenching of the ensemble of I_{fl} curves is dependent on the optical excitation intensity. As shown in Figure 4a, results with higher light intensities (red curve) show faster recovery times than those with lower excitation intensities (black curve). One explanation for this phenomenon is that the reduction rate of the new chemical state associated with deep traps (D^+) is substantially accelerated by optical excitation. Alternatively, charge transfer from a shallow site exciton (S^*) to D^+ could yield S^+ and D, thus effectively transforming a deep hole trap into a shallow trap. The data shown in Figure 4b, which compares the fluorescence recovery with and without optical excitation, indicate that the rates for deep trap reduction or untrapping might be extremely slow in the absence of light excitation. As can be seen in Figure 4c, the fluorescence quenching produced by the charging of the nanoparticles does not recover significantly, at $E = -0.15$ V, in the absence of light.⁵⁶

3.4. Model: Fluorescence-Quenching/Charging Relationship. To gain a better understanding of the EC charging processes in single molecules and nanoparticles, we constructed theoretical models and calculated the energies involved in charging these systems. In brief, the model system is constructed as a cluster of 1000 Lennard-Jones particles, each representing a chargeable unit. The interaction potential between these particles was set to give an average distance between particles of 1.4 nm. The configuration of the cluster was obtained through geometry optimization⁵⁷ and then held frozen for all subsequent calculations of electrostatic energies. To facilitate these electrostatic energy calculations, the cluster was embedded in a sphere of radius 9.2 nm with a dielectric constant of $\epsilon_p = 3.0$ (see Figure 5a). A fixed number of charges (holes) was then injected into the cluster at random monomer sites, and a Monte Carlo simulation was used to find the lowest-energy charge distribution. The total particle energy (E) is separated into the Coulombic part (E_{coul}) and the solvation part (E_{solv}). E_{coul} is calculated based on Coulomb's law for a given charge configuration in the medium of dielectric constant ϵ_p . The solvation term E_{solv} is defined as the energy change after replacing the dielectric constant outside the particle from ϵ_p to the solvent dielectric constant (ϵ_s) and deploying the counteranion in the first solvent shell of the particle. By assuming that the charge distribution is spherically symmetric, E_{solv} can be shown to have the following form^{58,59}

$$E_{\text{solv}} = \frac{q^2}{8\pi} \left[\frac{1}{R_{\text{sp}}} \left(\frac{1}{\epsilon_s} - \frac{1}{\epsilon_p} \right) - \frac{\beta}{(R_{\text{sp}} + r_s)\epsilon_s} \right] \quad (3)$$

where q is the number of charges; R_{sp} is the particle radius; and r_s is the solvent radius. The parameter $\beta = 1$ when electrolytes are present, otherwise $\beta = 0$.

During the sampling, charges were swapped between occupied and vacant sites and the resulting configuration accepted or rejected according to the Metropolis algorithm.⁶⁰ In all cases,

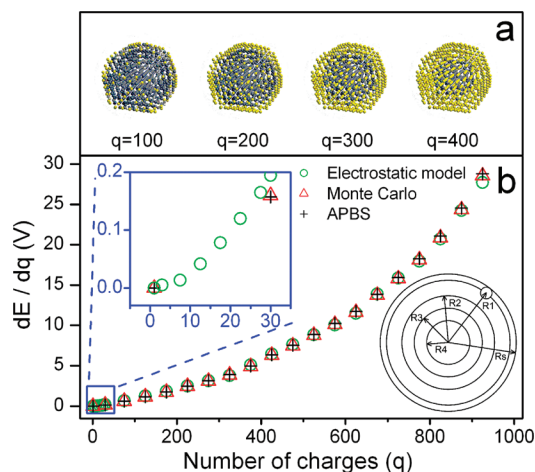


Figure 5. (a) Equilibrium charge distributions of a model solvated particle (big sphere, $R_s = 9.2$ nm) calculated using Monte Carlo simulations (see text for details). The particle contains 1000 oxidizable sites (small beads), and the charge distributions were calculated for fixed numbers of charges ($q = 100, 200, 300, 400$). The color represents the charge density of the oxidizable sites which scales from yellow ($q = 1$, charged) to black ($q = 0$, uncharged). (b) Finite difference of the system energy with respect to the number of charges calculated from the Monte Carlo simulations (black cross), APBS (red triangle), and electrostatic model (green circle) for the model particle shown in (a) in 0.1 M electrolyte solution. In the electrostatic model, four shells were considered as illustrated in the inset ($R_s = 9.20$, $R_1 = 7.21$, $R_2 = 6.06$, $R_3 = 4.91$, $R_4 = 3.75$ nm). The corresponding maximum occupancy for each shell: $q_1 = 368$, $q_2 = 273$, $q_3 = 182$, $q_4 < 177$.

the energy relaxed to its lowest level within 2×10^4 steps. The charge distributions and the system energies were obtained by averaging over a subsequent 10^5 configurations. The charge distributions for $q = 100, 200, 300$, and 400 are shown in Figure 5a.

When a polymer particle is in contact with an electrode, the bias potential (V) applied on the electrode is the driving force that oxidizes the polymer. At equilibrium, the total system energy (E_{tot}) is minimized at a given number of charges q

$$\frac{\partial E_{\text{tot}}}{\partial q} = \frac{\partial}{\partial q} [E(q) - V \cdot q] = 0 \quad (4)$$

Rewriting eq 4, we find the relation between the particle energy (E) and the bias potential as shown in eq 5

$$\frac{\partial E(q)}{\partial q} = V \quad (5)$$

In the following analysis, we calculate the finite difference of the particle energy with respect to the number of charges ($\partial E / \partial q$) to obtain the corresponding bias potential, which is at equilibrium with the charged particle. The $\partial E / \partial q$ curves calculated from our Monte Carlo simulations are shown in Figure 5b (black crosses). To test the validity of our model, we used the Adaptive Poisson–Boltzmann Solver⁶¹ (APBS) to calculate the total system energy for the most stable configurations obtained from the above Monte Carlo simulations. The Linearized Poisson–Boltzmann Equation was solved on a grid with a resolution of 1.769 Å to give the corresponding energy (E_{APBS}). The total system energy (E) is calculated according to the following equation and settings

$$E = E_{\text{APBS}}(\epsilon_s = 37.5, \epsilon_p = 3.0, [\text{Li}^+] = [\text{ClO}_4^-] = 0.1 \text{ M}) - E_{\text{APBS}}(\epsilon_s = 3.0, \epsilon_p = 3.0) + E_{\text{coul}}(\epsilon_s = 3.0, \epsilon_p = 3.0) \quad (6)$$

where E_{coul} is calculated directly from Coulomb's law. The first two terms on the right-hand-side eliminate the grid size dependence at the expense of two separate APBS energy evaluations. The corresponding $\partial E/\partial q$ curve is shown in Figure 5b (red triangle). These APBS results agree very well with the analytic approximation (eq 3) used in our Monte Carlo simulations (black cross).

The equilibrium charge distributions obtained from the Monte Carlo simulations show that charges are added to the cluster in shells, starting from the outermost shell and continuing inward. Thus, in principle, E_{coul} can be considered as the electrostatic energy of concentric charged shells. If q_i charges are distributed uniformly in the i th shell of radius R_i , according to the spherical charging model the total electrostatic energy (E_{coul}) is

$$E_{\text{coul}} = \sum_i \frac{q_i^2}{8\pi\epsilon_p R_i} + \sum_{i,j>i} \frac{q_i q_j}{4\pi\epsilon_p R_i} \quad (7)$$

However, the charges are not uniformly distributed, especially when the number of charges is small within a shell. Under these conditions, the electric field will deviate from the prediction of the spherical model. To take into account the localized nature of electrons in this model system, we can replace the first term in the right-hand side of eq 7 by an empirical formula derived for a shell with q_i distinct charges⁶²

$$E_{\text{coul}} = \sum_i \frac{0.5q_i^2 - 0.5523q_i^{3/2} + 0.0689q_i^{1/2}}{4\pi\epsilon_p R_i} + \sum_{i,j>i} \frac{q_i q_j}{4\pi\epsilon_p R_i} \quad (8)$$

The $\partial E/\partial q$ curve calculated from eq 3 and eq 8 is shown in Figure 5b (green circle). The excellent agreement with the above full-energy calculation result indicates that the simple coupled-spherical-capacitor model can accurately capture the energy profile of charging the spherical particle but with a much smaller calculation cost. This method is particularly useful for large clusters, when the full simulation becomes computationally expensive and thus practically unviable. Moreover, these calculations predict that the amount of charge in a model single molecule would change from $q = 0$ to $q = 30$ in a ~ 0.1 V bias window. This result is in good agreement with experimental results (see Figure 1 and Table 1), which show that a single molecule fluorescence intensity is quenched more than 98% from its initial value within a 0.1 V bias window. As mentioned before, previous experiments indicate that this degree of quenching is due to the injection of a small number of positive charges (<30) into the particle.

In Figure 6, the coupled-spherical-capacitor model was used to estimate the $\partial E/\partial q$ curve for a larger particle ($R_{\text{sp}} = 25$ nm). The spacing between shells and the maximal number of charges in each shell (see Figure 6 caption) were calculated based on a geometric factor which is estimated considering that a single charge is delocalized over 10 monomers⁶³ (creating an oxidizable site with radius: $10^{(1/3)} \times 0.7 \text{ nm} = 1.51 \text{ nm}$). The results from these calculations indicate that the potential necessary to charge a 25 nm particle to the point where $\sim 90\%$ of its

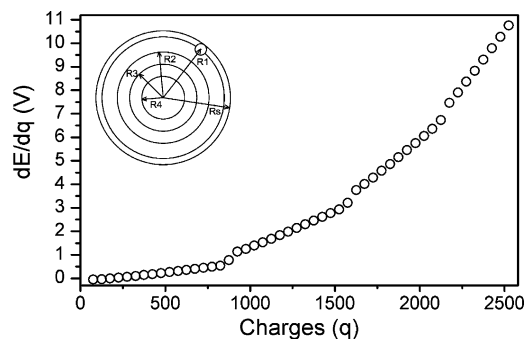


Figure 6. Finite difference of the system energy with respect to the number of charges calculated from the electrostatic model (solid circle) for the big model particle ($R_s = 25$ nm) in 0.1 M electrolyte solution. Four shells were considered in the calculation ($R_1 = 23.5$, $R_2 = 21.1$, $R_3 = 18.6$, $R_4 = 16.2$ nm). The corresponding maximum occupancy for each shell: $q_1 = 880$, $q_2 = 708$, $q_3 = 555$, $q_4 = 420$.

fluorescence is quenched is 11 V (from the bulk $E_{1/2}$). In this case, the fluorescence was estimated by summing up the fluorescence of all oxidizable sites. If a site is charged, it has no contribution to the total intensity. When a site is within the quenching radius ($R_q \sim 3.5$ nm) of n charged monomers, its fluorescence is reduced by $(1/2)^n$. These results are in contrast with the experimental results, which show >98% quenching of ~ 25 nm particles within 0.3 V from $E_{1/2,\text{film}}$ for particles well connected to the working electrode (see Section 3.3). A possible interpretation for this disagreement is that the charging of nanoparticles is facilitated by the penetration of ions and/or solvent molecules, which contribute to the stabilization and/or homogeneous distribution of the injected charges within the particle. In such a case, the penetration process presumably starts with the solvation of oxidized sites at the surface of the particle, which heavily screens the charge in this outer layer and facilitates the oxidation of the next layer of oxidizable sites. When the applied potential is above $E_{1/2}$, the process continues inward until most of the sites in the particle are oxidized. The ion and/or solvent penetration hypothesis is consistent with results from electrochemical-charging, fluorescence-quenching, and electrogenerated chemiluminescence experiments on relatively thick ($\sim 1 \mu\text{m}$) polymer films. These results will be included in a future publication. An alternative explanation for the apparent facile EC charging of polymer nanoparticles is that the formation of deep traps (vide supra) facilitates charging by lowering the effective $E_{1/2}$ of the whole particle. However, only a relatively small change on the effective $E_{1/2}$ can be assigned to the formation of deep traps, so this effect cannot explain the large discrepancy between theoretical and experimental results.

3.5. Low Voltage Modulation of the Fluorescence Quenching in Single Molecules. Interestingly, sweeping potentials in a range between ground state oxidation and reduction potentials cause a linear modulation of fluorescence intensities for all polymers studied *at the single molecule level* (results for F8BT are not shown). Figure 7 shows representative fluorescence-intensity transients and ensemble averaged decays for BEH-PPV and MEH-PPV molecules in a SMS-EC device scanned in a range of -0.4 to 0.4 V (vs AgQRE). As the potential was increased to 0.4 V, intensities increased linearly by $\sim 20\%$, and at negative potentials (-0.4 V), intensity decreases linearly by the same amount. All molecules showing modulation exhibit roughly the same modulation depth regardless of their emission intensity (which in most cases is correlated to the size of the molecule). The possible origins of this effect may involve (a) potential-dependent change in the refractive index of ITO, (b) electrolyte-induced quenching, (c) charge accumulation at the conjugated-polymer/ITO interface,

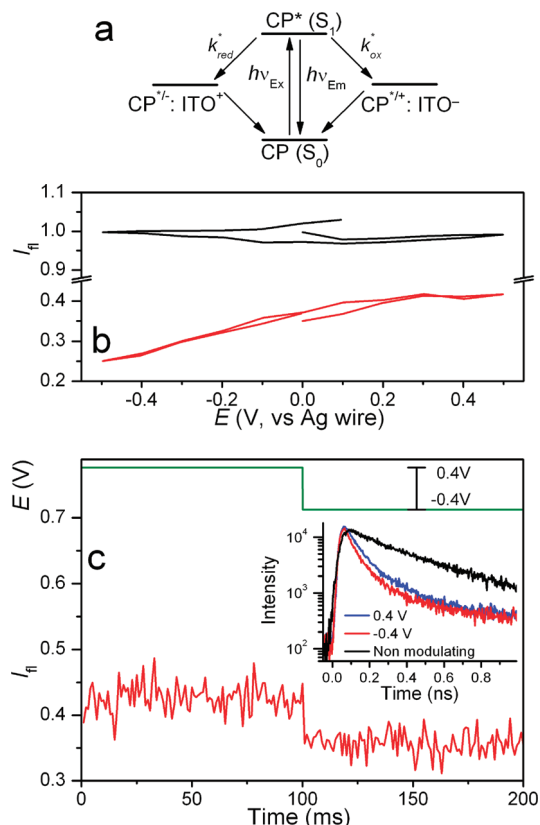


Figure 7. (a) States diagram for a conjugated polymer (CP) and ITO system. (b) Subensembles of single BEH-PPV molecule normalized fluorescence-intensity transients as a function of applied potential (scan rate of 1 V/s). The subensembles were constructed by sorting fluorescence transients that exhibit potential-dependent intensity modulation (red curve, 215 molecules) and transients that show no appreciable modulation (black curve, 4 molecules). Transients showing modulation are on average $\sim 65\%$ less intense than nonmodulating transients, and subensembles were scaled accordingly. (c) Ensemble average of ~ 100 single MEH-PPV molecules fluorescence intensity transients (red curve) obtained while applying the potential (vs Ag Wire) shown by the top green curve. The ensemble curve is scaled according to the average static quenching. Inset: ensemble emission decays obtained at potentials equal to: 0.4 V (red curve), -0.4 V (blue curve). The black curve corresponds to a subensemble corresponding to single molecules showing no potential-induced fluorescence modulation.

and (d) a change in excited state oxidation and reduction rate constants of the polymer (see Figure 7a).

Time-resolved, SMS-EC emission studies were used to unravel the underlying mechanism responsible for the linear, low-voltage intensity modulation effect. Upon contacting the ITO electrode, static quenching of polymer fluorescence (due to charge transfer) reduces emission yields by approximately 65% for polymers of comparable size and structure (MEH-PPV and BEH-PPV), as shown in Figure 7b,c. In addition, emission decays become nonexponential with an instrument limited fast component (~ 30 ps) that dominates the decay profile. Individual molecules showing no potential induced fluorescence modulation display a monoexponential fluorescence lifetime as shown by the black curve in the inset of Figure 7c. For molecules in contact with ITO, average lifetimes and emission yields vary by about $\pm 20\%$ from the values at 0 V when the potential is cycled within the -0.4 to 0.4 V range (red and blue curves in Figure 7c inset). As presented in the inset of Figure 7c, the fast decay component shows the largest change with applied potential suggesting that this emission component results from the CP–ITO interface.

TABLE 2: Comparison of Average Lifetimes and Intensities for Molecules on ITO and Glass Surfaces

sample	average lifetime (ps)	average intensity (counts/s)
MEH-PPV: 160 nm PS/glass	330 ± 66	2500 ± 1600
MEH-PPV: 160 nm PS/ITO	262 ± 1303	1320 ± 780
MEH-PPV: 20 nm PS/ITO	55 ± 32	1100 ± 2300

^a Samples consisted of the above thin films and substrates only. No electrolyte or applied bias was used in these measurements.

The mechanism of voltage-induced intensity modulation was explored by perturbing the device structure including the addition of oxide layers on ITO and thicker host matrix films and using larger polymer nanoparticles. Because all polymer materials studied showed linear intensity modulation at the single molecule level within the low voltage scan range, a possible source of this effect may simply be a potential-dependent change in the refractive index of ITO. However, this possibility can be ruled out since deposition of a thin electrical blocking layer of SiO₂ (~ 2 nm) over the ITO electrode resulted in the disappearance of the low voltage intensity modulation phenomena (not shown). This result was further corroborated using support matrices of varying thicknesses, and the data are summarized in Table 2. Thin films (i.e., 20 nm) showed a large number of molecules undergoing voltage-induced modulation in the (-0.4 to 0.4 V region), whereas thicker films (i.e., 160 nm) did not show significant modulation. The lack of appreciable intensity modulation in the thick film samples shows that a potential-dependent change in refractive index is not the cause for the low voltage intensity modulation phenomena.

The low voltage effect was also invariant of the choice of electrolyte, i.e., LiClO₄ or TBAClO₄ (data not shown). Furthermore, no modulation was observed upon substituting single molecules for larger polymer nanoparticles presumably due to the relatively small fraction of chromophores in close contact with the ITO electrode in the latter case. Accumulation of deeply trapped holes is another possible source for low voltage intensity modulation since mobile excitons should dissociate at these sites, which should also depend on the excitation rate (intensity) for generating excitons.⁶⁴ However, upon varying excitation intensity, no change in either modulation depth or behavior was observed for all materials studied (not shown).

The low voltage intensity modulation effect is putatively assigned as a potential-dependent alteration of competing excited state oxidation and reduction processes shown schematically in Figure 7a. Since both excited state oxidation and reduction mechanisms are capable of quenching polymer emission, we use arguments based on potential-dependent driving forces to rationalize the observed trends in the data. For example, increasing potentials from 0 to 0.4 V results in an increase in driving force for excited state oxidation, which should lead to a larger rate constant for this process (k_{ox}^* , see Figure 7a) thus a higher quenching of the emission. Conversely, the application of potentials more positive than 0 V decreases the excited state reduction driving force causing a decrease of the related rate constant (k_{red}^*) thus increasing the observed emission intensity. On the basis of the observed trend in Figure 7, it is apparent that potential-induced modulation of the excited state reduction processes (i.e., electron transfer from ITO to the polymer) dominates the low-potential fluorescence-modulation effect.

4. Conclusions

Using SMS-EC, we have observed the presence of a narrow distribution of states ($\sigma = 0.04$ V) in the low-energy edge of

the redox accessible density of states of the conjugated polymer BEH-PPV in contact with an ITO electrode. Experiments on BEH-PPV nanoparticle samples having different host polymer layers show that oxidation and fluorescence quenching occurs over a narrow potential range for particles in good contact with the EC double layer. In contrast to this, when particles are sufficiently separated from the EC double layer, oxidation occurs slowly relative to the time scale of the experiment (<60 s). A combination of Monte Carlo simulations and application of Poisson–Boltzmann solvers was used to model the charging of single molecules and nanoparticles in the electrochemical environment. The results indicate that the penetration of solvent and/or ions into the polymer nanoparticles is necessary to achieve the observed fluorescence-quenching/charging over a ~0.1 V range of EC potentials. Finally, single-molecule fluorescence-lifetime and SMS-EC techniques were used to unravel the mechanism responsible for the linear, low-potential intensity modulation effect observed in conjugated polymer single molecules in contact with ITO. The results indicate that potential-induced modulation of the excited state reduction processes (i.e., electron transfer from ITO to the polymer) dominates the low-potential fluorescence-modulation effect. In general, the experiments performed confirm the ability of SMS-EC to unravel complex charge transport processes at organic–inorganic interfaces at the nanoscale.

Acknowledgment. This work was supported by the National Science Foundation and the Welch Foundation (PFB and GH).

References and Notes

- Zhu, X. Y. *J. Phys. Chem. B* **2004**, *108*, 8778.
- Cahen, D.; Kahn, A. *Adv. Mater.* **2003**, *15*, 271.
- Halls, J. J. M.; Cornil, J.; dos Santos, D. A.; Silbey, R.; Hwang, D. H.; Holmes, A. B.; Bredas, J. L.; Friend, R. H. *Phys. Rev. B: Condens. Matter Mater. Phys.* **1999**, *60*, 5721.
- Fahlman, M.; Crispin, A.; Crispin, X.; Henze, S. K. M.; de Jong, M. P.; Osikowicz, W.; Tengstedt, C.; Salaneck, W. R. *J. Phys.: Condens. Matter* **2007**, *19*.
- Fahlman, M.; Crispin, A.; Crispin, X.; Henze, S. K. M.; de Jong, M. P.; Osikowicz, W.; Tengstedt, C.; Salaneck, W. R. *J. Phys.: Condens. Matter* **2007**, *19*, 183202 (20p).
- Friend, R. H.; Gymer, R. W.; Holmes, A. B.; Burroughes, J. H.; Marks, R. N.; Taliani, C.; Bradley, D. D. C.; Dos Santos, D. A.; Bredas, J. L.; Logdlund, M.; Salaneck, W. R. *Nature (London)* **1999**, *397*, 121.
- Seeley, A. J. A. B.; Friend, R. H.; Kim, J.-S.; Burroughes, J. H. *J. Appl. Phys.* **2004**, *96*, 7643.
- Salaneck, W. R.; Stafstroem, S.; Bredas, J. L., Eds. *Conjugated Polymer Surfaces and Interfaces: Electronic and Chemical Structure of Interfaces for Polymer Light Emitting Devices*; 1996.
- Brabec, C. J.; Sariciftci, N. S.; Hummelen, J. C. *Adv. Funct. Mater.* **2001**, *11*, 15.
- Wohrle, D.; Meissner, D. *Adv. Mater.* **1991**, *3*, 129.
- Friend, R. H.; Gymer, R. W.; Holmes, A. B.; Burroughes, J. H.; Marks, R. N.; Taliani, C.; Bradley, D. D. C.; Dos Santos, D. A.; Bredas, J. L.; Logdlund, M.; Salaneck, W. R. *Nature* **1999**, *397*, 121.
- Dimitrakopoulos, C. D.; Malenfant, P. R. L. *Adv. Mater.* **2002**, *14*, 99.
- Horowitz, G. *Adv. Mater.* **1998**, *10*, 365.
- Berggren, M.; Richter-Dahlfors, A. *Adv. Mater.* **2007**, *19*, 3201.
- Ghosh, S.; Ingnas, O. *J. Electrochem. Soc.* **2000**, *147*, 1872.
- Bard, A. J.; Faulkner, L. R. *Electrochemical Methods: Fundamentals and Applications*; 2001.
- Inzelt, G. *Electroanal. Chem.* **1994**, *18*, 89.
- Bacskaï, J.; Inzelt, G. *J. Electroanal. Chem.* **1991**, *310*, 379.
- Barbero, C.; Calvo, E. J.; Etchenique, R.; Morales, G. M.; Otero, M. *Electrochim. Acta* **2000**, *45*, 3895.
- Kaufman, F. B.; Schroeder, A. H.; Engler, E. M.; Kramer, S. R.; Chambers, J. Q. *J. Am. Chem. Soc.* **1980**, *102*, 483.
- Oyama, N.; Ohsaka, T. *Prog. Polym. Sci.* **1995**, *20*, 761.
- Campbell, D. J.; Herr, B. R.; Hulteen, J. C.; VanDuyne, R. P.; Mirkin, C. A. *J. Am. Chem. Soc.* **1996**, *118*, 10211.
- Gettinger, C. L.; Heeger, A. J.; Drake, J. M.; Pine, D. J. *J. Chem. Phys.* **1994**, *101*, 1673.
- Andersson, M. R.; Yu, G.; Heeger, A. J. *Synth. Met.* **1997**, *85*, 1275.
- Gustafsson, G.; Cao, Y.; Treacy, G. M.; Klavetter, F.; Colaneri, N.; Heeger, A. J. *Nature* **1992**, *357*, 477.
- Chen, L. X.; Jager, W. J. H.; Gosztola, D. J.; Niemczyk, M. P.; Wasielewski, M. R. *Effects of chemical modifications on photophysics and exciton dynamics of pi-conjugation attenuated and metal-chelated photoconducting polymers*; 2001.
- Palacios, R. E.; Fan, F.-R. F.; Bard, A. J.; Barbara, P. F. *J. Am. Chem. Soc.* **2006**, *128*, 9028.
- Palacios, R. E.; Fan, F. R. F.; Grey, J. K.; Suk, J.; Bard, A. J.; Barbara, P. F. *Nat. Mater.* **2007**, *6*, 680.
- Chang, Y. L.; Palacios, R. E.; Fan, F. R. F.; Bard, A. J.; Barbara, P. F. *J. Am. Chem. Soc.* **2008**, *130*, 8906.
- Lang, D. V.; Chi, X.; Siegrist, T.; Sergent, A. M.; Ramirez, A. P. *Phys. Rev. Lett.* **2004**, *93*, 076601/1.
- Salleo, A.; Street, R. A. *Phys. Rev. B: Condens. Matter Mater. Phys.* **2004**, *70*, 235324/1.
- Muller, E. M.; Marohn, J. A. *Adv. Mater. (Weinheim, Germany)* **2005**, *17*, 1410.
- Campbell, A. J.; Bradley, D. D. C.; Antoniadis, H. *Appl. Phys. Lett.* **2001**, *79*, 2133.
- Jaquith, M.; Muller, E. M.; Marohn, J. A. *J. Phys. Chem. B* **2007**, *111*, 7711.
- Coffey, D. C.; Ginger, D. S. *Nat. Mater.* **2006**, *5*, 735.
- Sinha, S.; Monkman, A. P. *J. Appl. Phys.* **2005**, *97*.
- Northrup, J. E.; Chabinyc, M. L. *Phys. Rev. B* **2003**, *68*.
- Kadashchuk, A.; Schmechel, R.; von Seggern, H.; Scherf, U.; Vakhnin, A. *J. Appl. Phys.* **2005**, *98*, 024101/1.
- Sinha, S.; Monkman, A. P. *J. Appl. Phys.* **2005**, *97*, 114505 (7p).
- Northrup, J. E.; Chabinyc, M. L. *Phys. Rev. B* **2003**, *68*, 041202 (4p).
- Neef, C. J.; Ferraris, J. P. *Macromolecules* **2000**, *33*, 2311.
- Gutierrez, J. J.; Luong, N.; Zepeda, D.; Ferraris, J. P. *Synthesis of diblock, triblock, and star copolymers of PPV derivatives: A route to donor-acceptor blocks*; 2004.
- Ferraris, J. P.; Gutierrez, J. J. *U.S. Patent* 2006; Vol. 7, p 135.
- Szymanski, C.; Wu, C.; Hooper, J.; Salazar, M. A.; Perdomo, A.; Dukes, A.; McNeill, J. J. *J. Phys. Chem. B* **2005**, *109*, 8543.
- Wu, C.; Peng, H.; Jiang, Y.; McNeill, J. J. *J. Phys. Chem. B* **2006**, *110*, 14148.
- Palacios, R. E.; Lee, K. J.; Rival, A.; Adachi, T.; Bolinger, J. C.; Fradkin, L.; Barbara, P. F. *Chem. Phys.* **2009**, *357*, 21.
- Bolinger, J. C.; Fradkin, L.; Lee, K.-J.; Palacios, R. E.; Barbara, P. F. *Proc. Natl. Acad. Sci. U.S.A.* **2009**, *106*, 1342.
- Gesquiere, A. J.; Park, S. J.; Barbara, P. F. *J. Phys. Chem. B* **2004**, *108*, 10301.
- Park, S.-J.; Gesquiere, A. J.; Yu, J.; Barbara, P. F. *J. Am. Chem. Soc.* **2004**, *126*, 4116.
- Yu, J.; Song, N. W.; McNeill, J. D.; Barbara, P. F. *Isr. J. Chem.* **2004**, *44*, 127.
- Lammi, R. K.; Barbara, P. F. *Photochem. Photobiol. Sci.* **2005**, *4*, 95.
- Hu, D.; Yu, J.; Padmanaban, G.; Ramakrishnan, S.; Barbara, P. F. *Nano Lett.* **2002**, *2*, 1121.
- Manoj, A. G.; Narayan, K. S.; Gowri, R.; Ramakrishnan, S. *Synth. Met.* **1999**, *101*, 255.
- Oliveira, F. A. C.; Cury, L. A.; Righi, A.; Moreira, R. L.; Guimaraes, P. S. S.; Matinaga, F. M.; Pimenta, M. A.; Nogueira, R. A. *J. Chem. Phys.* **2003**, *119*, 9777.
- Woo, H. S.; Lhost, O.; Graham, S. C.; Bradley, D. D. C.; Friend, R. H.; Quattrocchi, C.; Bredas, J. L.; Schenk, R.; Muellen, K. *Synth. Met.* **1993**, *59*, 13.
- Bolinger, J.; Fradkin, L.; Lee, K.-J.; Palacios, R. E.; Barbara, P. F. *Proc. Natl. Acad. Sci. U.S.A.* **2009**, *106*, 1342.
- Wales D. J.; Doye J. P. K.; Dullweber A.; Hodges M. P.; Naumkin F. Y.; Calvo F.; Hernández-Rojas J.; Middleton T. F. The Cambridge Cluster Database, URL <http://www-wales.ch.cam.ac.uk/CCD.html>.
- Boettcher, C. J. F. *Theory of Electric Polarization: Dielectrics in Time-Dependent Fields*, 2nd ed.; Elsevier Science Ltd: New York, 1980.
- Jackson, J. D. *Classical Electrodynamics*, 3rd ed.; Wiley: New York, 1998.
- Frenkel, D.; Smit, B. *Understanding Molecular Simulation: From Algorithms to Applications*, 2nd ed.; Academic Press: Boston, 2002.
- Baker, N. A.; Sept, D.; Joseph, S.; Holst, M. J.; McCammon, J. A. *Proc. Natl. Acad. Sci. U.S.A.* **2001**, *98*, 10037.
- Rakhmanov, E. A.; Saff, E. B.; Zhou, Y. M. *Computational Methods and Function Theory*; Ali, R. M., Ruscheweyh, S., Saff, E. B., Eds.; World Scientific: Singapore, 1995; p 111.
- The size of a monomer is estimated as a sphere of 0.7 nm in radius based on simple molecular modeling using Chem3D Ultra 8.0.
- McNeill, J. D.; O'Connor, D. B.; Adams, D. M.; Barbara, P. F.; Kaemmer, S. B. *J. Phys. Chem. B* **2001**, *105*, 76.